Templated Growth and Passivation of Vertically Oriented Antimony Selenide Thin Films for High-Efficiency Solar Cells in Substrate Configuration

Suman Rijal, Deng-Bing Li, Rasha A. Awni, Chuanxiao Xiao, Sandip S. Bista, Manoj K. Jamarkattel, Michael J. Heben, Chun-Sheng Jiang, Mowafak Al-Jassim, Zhaoning Song, and Yanfa Yan**

S. Rijal, D.-B. Li, R. A. Awni, S. S. Bista, M. K. Jamarkattel, M. J. Heben, Z. Song, and Y. Yan

Wright Center for Photovoltaics Innovation and Commercialization, Department of Physics and Astronomy, The University of Toledo, OH 43606, USA
E-mail: zhaoning.song@utoledo.edu (Z.S.), yanfa.yan@utoledo.edu (Y.Y.)

C. Xiao, C.-S. Jiang, M. Al-Jassim,

Materials Science Center, National Renewable Energy Laboratory, Golden, CO, USA

Keywords: antimony selenide, solar cells, seed layers, annealing, passivation, activation energy

Antimony Selenide (Sb_2Se_3) is a promising low-cost photovoltaic material with a one-dimensional crystal structure. The grain orientation and defect passivation play a critical role in determining the performance of polycrystalline Sb_2Se_3 thin-film solar cells. Here, we introduce a seed layer on a molybdenum (Mo) substrate to template the growth of a vertically oriented, columnar Sb_2Se_3 absorber layer by closed space sublimation. By controlling the grain orientation and compactness of the Sb_2Se_3 seeds, we obtain high-quality Sb_2Se_3 absorber layers with passive Sb_2Se_3/Mo interfaces, which in turn improve the transport of photoexcited charge carriers through the absorber layer and its interfaces. We further utilize post-deposition annealing of absorber layers in ambient air to passivate the defects in Sb_2Se_3 and enhance the quality of the front heterojunction. As a result of systematic processing optimization, we fabricate Sb_2Se_3 planar heterojunction solar cells in substrate configuration with a champion power conversion efficiency of 8.5%.

1. Introduction

Antimony selenide (Sb_2Se_3) is emerging as a promising alternative photovoltaic (PV) absorber material to conventional semiconductors, such as silicon (Si), cadmium telluride (CdTe) and cooper indium gallium selenide ($Cu(In,Ga)Se_2$), because of its suitable bandgap of 1.1-1.3 eV, high absorption coefficients of ~10^5 cm^{-1}, low toxicity, low cost, and earth-abundant nature.[1-2] It has a simple binary composition which provides for much simpler growth with reduced probability for secondary phase formation as is a common problem in $Cu_2ZnSn(S,Se)_4$ and any other ternary Cu chalcogenide compounds.[3-4] As compared to other emerging PV devices, such as dye-sensitized solar cells, organic PVs, and metal halide perovskite solar cells, Sb_2Se_3 solar cells are robust and more stable in ambient air and may be able to avoid the need for sophisticated encapsulation.[5]

In a short period of time, Sb_2Se_3 solar cells have shown a promising learning curve. The record power conversion efficiency (PCE) increased rapidly from 2.1% in 2014 to 9.2% in 2019.[6-7] However, the PCE of Sb_2Se_3 solar cells is still very far below the corresponding thermodynamic efficiency limit of > 30%,[8] leaving plenty of room for improvement. Studies have shown that the one-dimensional (1D) crystal orientation of Sb_2Se_3 grains and the intrinsic defects in the bulk and at the interfaces dictate the PV performance of Sb_2Se_3 solar cells.[9-11] The grain orientation determines the charge transport and defect properties throughout the absorber layer. The 1D ribbon-like structures of Sb_2Se_3 can assist in efficient charge transport if the ribbons are aligned perpendicular to the substrate.[10] The bulk and interfacial defects act as recombination centers and limit the open-circuit voltage (V_{OC}), fill factor (FF), and device performance.[12] Many research efforts have been directed toward improving the quality of Sb_2Se_3 absorber layers, by advancing deposition methods,[13-14] doping engineering,[15-16] and post-annealing treatments.[17-21] Meanwhile, a variety of interface engineering strategies were developed to reduce interface recombination and improve the V_{OC} and PCE, including surface treatment to induce grain boundary (GB) inversion,[22] introduction of tunable buffer layers,[23] and management of buffer/absorber band energy alignment.[24]

Seed layer assisted growth has been employed to obtain the desired crystal orientation and bulk defect properties of Sb_2Se_3 films deposited on metal oxide layers, consequently improving the performance of solar cells in superstrate configuration. Huntter et al. first introduced a seed layer in the preparation of superstrate Sb_2Se_3 solar cells by two-step closed space sublimation (CSS).[25] Kondrotas et al. further studied the growth mechanism of Sb_2Se_3 thin films by a vapor

transport deposition method and found three growth regimes by varying the substrate and source temperatures.[26] Li et al. studied the impact of introducing a seed layer between TiO_2 and Sb_2Se_3 on improving the interface properties and promoting oriented crystal growth, which enabled 7.6% efficient Sb_2Se_3 solar cells in n-i-p superstrate structure.[10] Shen et al. demonstrated a 7.5% efficiency for Sb_2Se_3 solar cells in superstrate configuration using a seed layer assisted CSS method.[11] Despite the success in superstrate configuration Sb_2Se_3 solar cells, the seed layer assisted growth has rarely been implemented on molybdenum (Mo) layers for efficient substrate type devices.

In addition to the grain orientation control, the passivation of the bulk and interfacial defects is essential to suppress the recombination in Sb_2Se_3 solar cells and to achieve high efficiency devices. Oxygen passivation is found to be a ubiquitous and simple strategy for a variety of chalcogenide thin-film solar cells.[28-31] Various oxygen passivation strategies have been applied to Sb_2Se_3 solar cells.[5, 12, 32] For instance, Liu et al. introduced controlled oxygen during the Sb_2Se_3 film growth and improved the PCE of superstrate Sb_2Se_3 devices to over 4%.[12] Fleck et al. studied how exposure to air increased the efficiency of superstrate Sb_2Se_3 solar cells to 5.87% via a reduction in the back contact barrier height.[5] However, there remains a need for a facile oxygen treatment for improving the performance of substrate configuration Sb_2Se_3 solar cells.

Here, we fabricate substrate-type Sb_2Se_3 solar cells using a CSS setup built in-house (Figure S1). We first introduce a seed layer on a Mo substrate by rapid thermal evaporation (RTE) to enable the templated growth of a vertically orientated Sb_2Se_3 seed layer, which not only facilitates the growth of high-quality Sb_2Se_3 absorber layer with high crystallinity, large columnar grains, and preferred orientation but also avoids the void formation at the back interface. We further employ facile post-deposition annealing in ambient air to passivate the bulk defects in the Sb_2Se_3 absorber layer. The passivation effect is verified by admittance spectroscopy measurements, which show removal of some defects and shallower defect activation energies after annealing in the air. Additionally, scanning probe microscopy measurements show the slightly reduced conductivity and increased the top surface potential of the films after air annealing, benefiting the charge extraction at the front heterojunction. As a result, we fabricate Sb_2Se_3 solar cells with a champion efficiency of 8.5%, which is the highest reported efficiency to date for Sb_2Se_3 planar heterojunction solar cells (Table S1).

2. Result and Discussion

2.1. Seeded Growth of Vertically Oriented Sb2Se3 Films

The crystallinity and orientation of polycrystalline Sb_2Se_3 thin films is particularly important because of their anisotropic optical and electrical properties.[33] The seed layer plays a crucial role in controlling the crystalline quality and preferred orientation of Sb_2Se_3 thin films and their interface properties.[10] It is known that for Sb_2Se_3, the growth of 1D $(Sb_4Se_6)_4$ ribbons can be oriented in mainly two groups of directions with respect to the substrate surface, i.e., the lying ribbons with their [hk0] directions being perpendicular to the substrate surface **(Figure 1a)** and the standing ribbons with their [hkl, l≠0] directions being perpendicular to the substrate surface (Figure 1b), depending on growth conditions such as substrate temperature, source temperature, and pressure.[14, 17, 34] In the film growth direction, the lying ribbon crystals oriented in [hk0] are terminated with fully saturated Se atoms. Therefore, the ribbons are bonded by the weak Van der Waals force (Figure 1a), whereas standing crystals oriented in [hkl, l≠0] are terminated by atoms with unsaturated atoms (either Sb or Se atoms) that can potentially form strong chemical bonds with functional contact materials (Figure 1b).[10] When ribbons are orientated in the [hkl, l≠0] directions, charge carriers can be easily transported through the interface owing to the strong chemical bonds.[17] In contrast, charge transport along the [hk0] directions needs to overcome the interchain barriers, which is less efficient. Thus, the [hkl, l≠0] are the preferred orientations that benefit the transport of photoexcited carriers and, consequently, the device performance of Sb_2Se_3 solar cells.

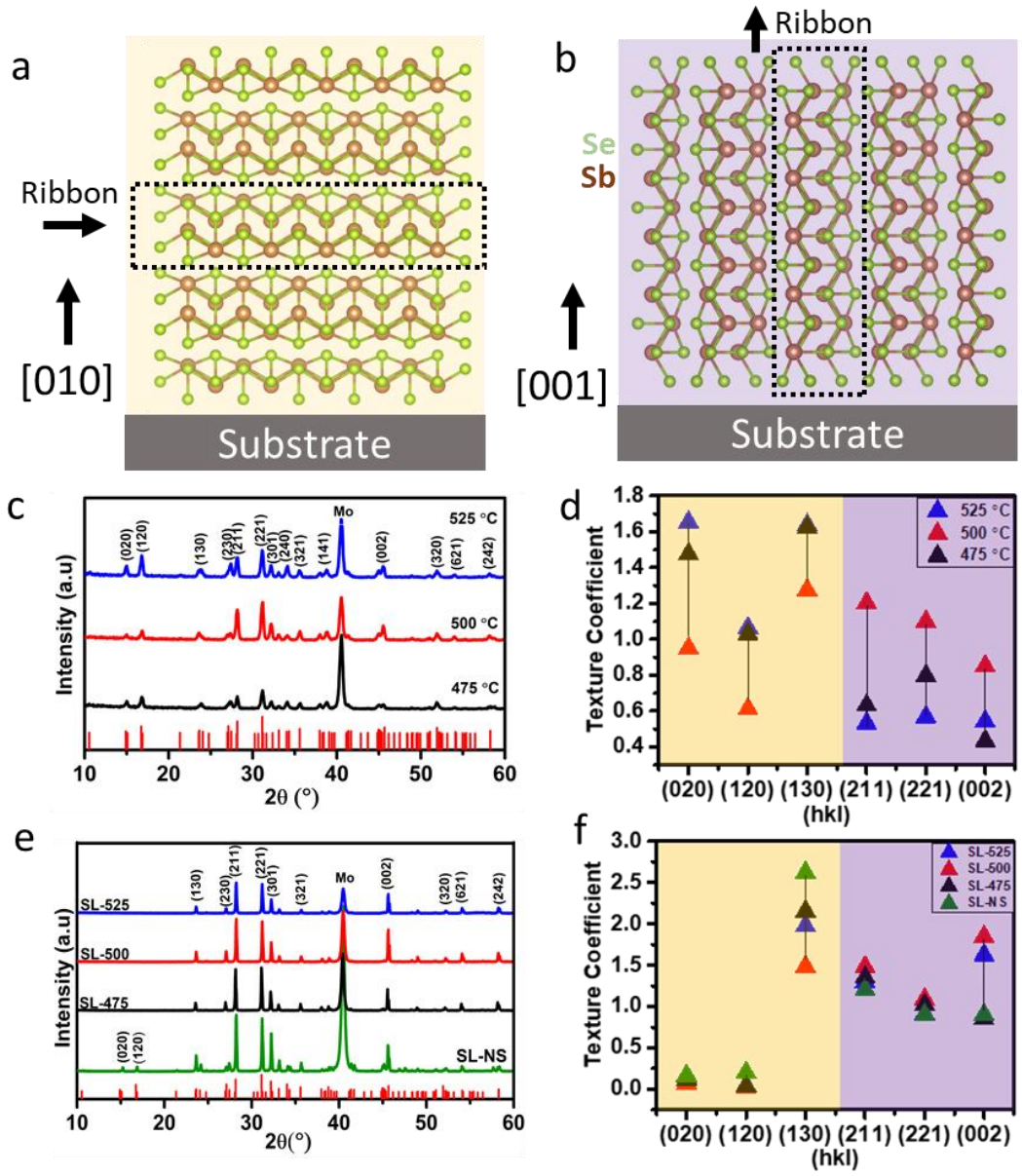

Figure 1. Structural properties of Sb_2Se_3 thin films. Crystal structures of Sb_2Se_3 in the (a) [010] and (b) [001] orientations. (c) XRD patterns and (d) texture coefficients of Sb_2Se_3 seed layers grown on Mo at different source temperatures. (e) XRD patterns and (f) texture coefficients of Sb_2Se_3 absorber layers grown on different seed layers. Note that the yellow region represents the peaks for horizon ribbons, whereas the purple region represents the peaks for vertical ribbons.

To prepare Sb_2Se_3 films with the preferred crystal orientations, we introduce a template seed layer on a Mo substrate by using RTE. The morphology and structural properties of Sb_2Se_3 seed layers deposited at different source temperatures (T_{sou}) were characterized by scanning electron microscopy (SEM) and X-ray diffraction (XRD). Figure S2 shows a series of top-view and

cross-sectional SEM images of Sb_2Se_3 seed layers grown on Mo substrates at different temperatures, exhibiting the morphological evolution of Sb_2Se_3 seed layers as a function of T_{sou}. At T_{sou} = 475 °C, loosely packed and randomly oriented grains with ribbon-like structures were formed. When T_{sou} was increased to 500 °C, the seed layer became more compact, and the ribbon grains were oriented mainly along the vertical direction. Further increasing T_{sou} to 525 °C led to the formation of a dense layer of randomly oriented ribbon grains. Energy dispersive X-ray spectroscopy (EDS) measurements (Table S2) show that all the seed layers are Se rich. Because the partial vapor pressure of Se is much lower than that of the Sb, it is critical to deposit the seed layer at a rapid temperate ramp rate to the desired temperature to preserve the Se-rich stoichiometry.

The changes in the crystal orientation of the Sb_2Se_3 seed layers with T_{sou} can be measured by analyzing the XRD data, as shown in Figure 1c. Among the seed layers grown at different temperatures of 475, 500, and 525 °C, the film deposited at 500 °C exhibits the lowest intensities for the undesired (020), (120), and (130) peaks and the highest intensities for the preferred (211), (221), and (002) peaks. We further quantified the crystal orientation changes by the texture coefficients (TC) for the (020), (120), (130), (221), (211), and (002) peaks using the following equation:

$$TC(hkl) = \frac{\frac{I(hkl)}{I_o(hkl)}}{\sum_{i=1}^{N} \frac{I(h_i k_i l_i)}{I_o(h_i k_i l_i)}} \quad (1)$$

where $I(hkl)$ and $I_o(hkl)$ are the diffraction peak intensities of the (hkl) planes in the measured and standard XRD patterns of Sb_2Se_3 (JCPDS 97-008-5676), respectively. The texture coefficient analysis of the seed layers (Figure 1d) confirms that the 500 °C deposited seed layer has preferred orientations in the [hkl, l≠0] directions. Increasing the [hkl, l≠0] orientation and reducing the [hk0] orientation can be explained by the adhesion force between the Sb_2Se_3 ribbon grains and the Mo substrate. Sb_2Se_3 grains in the [hk0] directions are bonded to the substrates via a weak Van der Waals force, while grains in the [hkl, l≠0] directions are bonded to the substrate via a stronger chemical bonding. At a low temperature (475 °C), the deposition rate is low, and the individual grains with all the orientations can randomly grow on the substrates. At a higher temperature (500 °C), the [hk0]-oriented grains are more easily to break down the adhesion and evaporate from the Mo substrate, leaving behind a seed layer with more strongly bonded [hkl, l≠0]-oriented grains. Further increasing the temperature to 525 °C

leads to the rapid formation of a densely packed layer consisting of randomly oriented grains due to a higher deposition rate.

Figure 1e compares the XRD patterns of the Sb_2Se_3 absorber layers prepared on the seed layers deposited at different temperatures and a Sb_2Se_3 absorber layer deposited without a seed layer as a reference. The Sb_2Se_3 film prepared without a seed layer (SL-NS) consists of the unfavorable (020) and (120) peaks, consistent with the seed layers directly grown on Mo substrates. Interestingly, Sb_2Se_3 films grown on top of the seed layer templates are absent of these undesired peaks. The results indicate that the weakly bonded [hk0] horizontal ribbons were not stabilized on the substrate and could reorient during the deposition of bulk Sb_2Se_3 films. A comparison of the XRD peaks among the Sb_2Se_3 films grown on different seed layers deposited at 475, 500, and 525 °C (referred to as SL-475, SL-500, and SL-525, respectively) reveals that the preferred peaks (211), (221), and (002) of the SL-500 sample has the highest intensity. Figure 1f shows that the TC analysis of these Sb_2Se_3 films. The SL-500 sample exhibits the highest TCs for the desired (211), (221), and (002) peaks (purple background) and lowest values for the undesired (hk0) peaks (yellow background). The results confirm that the templated growth based on Sb_2Se_3 seed layers helps orient the grains in the preferred directions.

Figure 2a-h displays the top-view and cross-sectional SEM images of the bulk Sb_2Se_3 absorber layers grown without a seed layer or on various seed layers deposited at different temperatures. Figure 2a shows that the Sb_2Se_3 absorber layer grown without a seed layer has a nonuniform morphology with a high degree of porosity. Figure 2b-d shows that Sb_2Se_3 absorber layers grown on a seed layer are more compact and uniform than those without a seed layer. Figure S3 shows the histogram analysis of grain size under different seed layer conditions. The grain size increases and void density decreases when the seed layer deposition temperature increases from 475 to 500 °C, but the trend is reversed when the temperature increases to 525 °C. The 500 °C sample shows the largest average grain size of 1.56 μm (Figure S3-c).

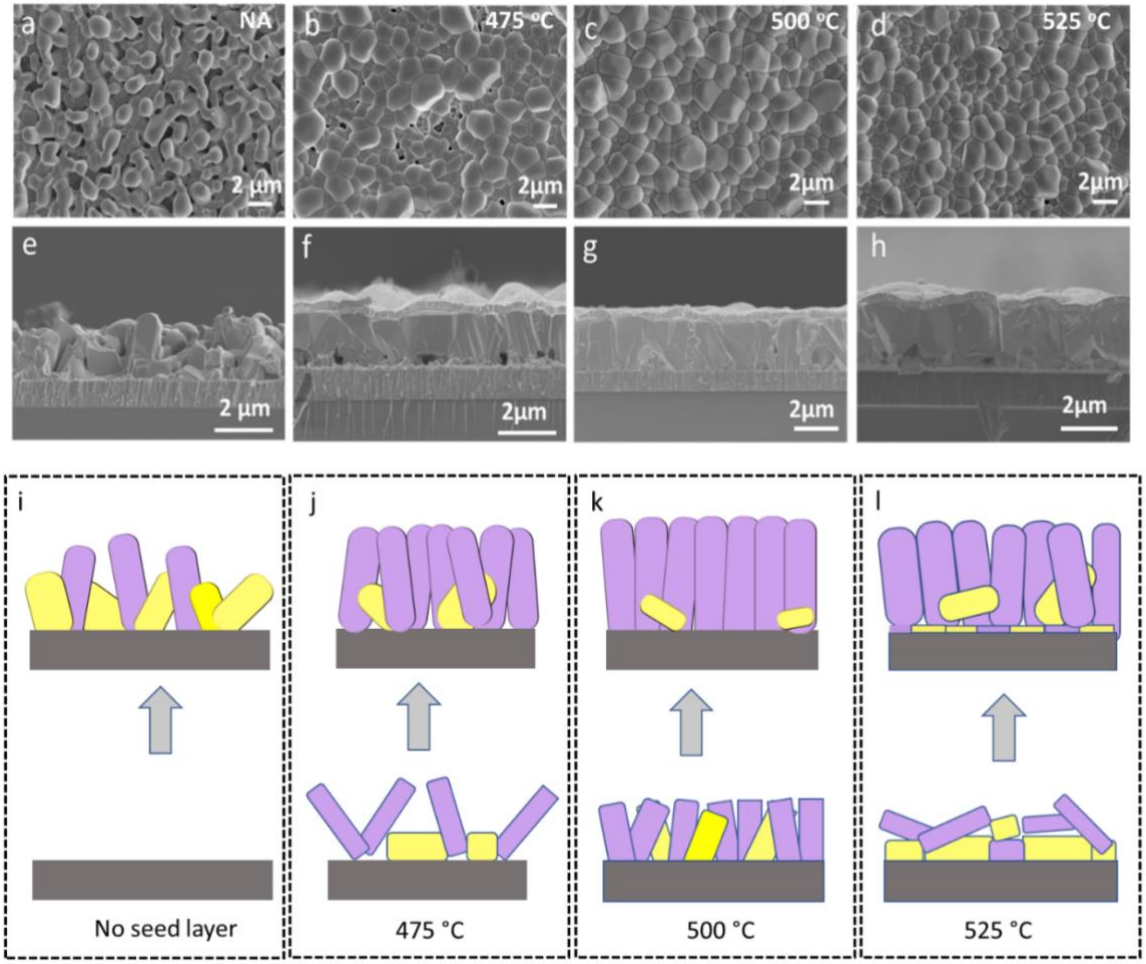

Figure 2. Templated growth of Sb_2Se_3 thin films on different seed layers. (a-d) plane view SEM images of Sb_2Se_3 thin films grown (a) without seed layer and on seed layers deposited at (b) 475 °C, (c) 500 °C, and (d) 525 °C, respectively. (e-h) Corresponding cross-sectional images of Sb_2Se_3 films grown on different seed layers. (i-l) Schematic illustrations of templated growth of Sb_2Se_3 thin films.

The seed layer also significantly influences the interfacial adhesion between the Sb_2Se_3 absorber layer and Mo back electrode. The cross-sectional SEM images (Figure 2e-h) show that the Sb_2Se_3/Mo interface became more compact and void-less after introducing the seed layer. The 475 °C sample still exhibits a high density of pores at the interface (Figure 2f), whereas the 500 °C sample is completely void-free (Figure 2g). Unlike other films, the 525 °C sample shows a bi-layer structure consisting of a thin small-grained underlying layer and a thicker large-grained upper layer (Figure 2h). The growth process of the seed layer and absorber can simply be described by the schematics of the growth shown in Figure 2i-l. The direct deposition of Sb_2Se_3 on Mo results in randomly oriented and loosely packed grains (Figure 2i), due to the relatively low free energies for the nucleation of all the crystal orientations. The seed layer

grown at 475 °C is discontinuous and randomly aligned (Figure 2j). When the Sb_2Se_3 absorber layer is deposited, some traces of the seed layer are left over at the interface, while most of the seed grains recrystallize and merge with the absorber layer and reorient in the perpendicular direction. The seed layer deposited at 500 °C is compact and mainly oriented in the desired [hkl, l≠0] directions (Figure 2k). The seed grains grow to larger sizes after the deposition of the bulk absorber layer, retaining mostly in the [hkl, l≠0] orientations. The seed layer deposited at 525 °C comprises densely packed and randomly oriented seed grains (Figure 2i). Owing to the strong intralayer adhesion, the seed layer structure is preserved after growing the bulk absorber layer, resulting in a distinct bi-layer structure. The presence of a bi-layer structure in the absorber layer is typically detrimental to device performance because it may hinder the charge transport and introduce non-radiative recombination.

To investigate the impact of the seed layer growth condition on solar cell performance, we fabricated substrate-type Sb_2Se_3 solar cells with a structure of glass/Mo/Sb_2Se_3/CdS/i-ZnO/AZO/Ag grid. The Sb_2Se_3 absorber layers were deposited with different seed layer conditions and selenized after the deposition (see the Experimental Section for details). **Figure 3a** shows the J-V curves of the best-performing cells from each group of devices. Their corresponding PV parameters are summarized in **Table 1**. The SL-500 device shows the highest PCE of 7.47%, with high open-circuit voltage (V_{OC}), short-circuit current density (J_{SC}), and fill factor (FF) of 459 mV, 26.54 mA cm^{-2}, and 61.39%, respectively. The other two devices, SL-475 and SL-525, show lower values for all the PV parameters. The SL-475 device suffers severely from high series resistance (R_S) and low shunt resistance (R_{SH}), which are mainly attributed to a high proportion of the undesired [hk0] oriented grains and the voids at the Sb_2Se_3/Mo interface. The horizontal ribbon grains with the [hk0] orientations are more likely to introduce non-radiative recombination centers at the GBs, resulting in an overall low external quantum efficiency (EQE) for the SL-475 sample (Figure 3b) and a low V_{OC} of 412 mV. The SL-525 device shows improved V_{OC} and J_{SC} compared with SL-475 but is adversely affected by the misaligned interface layer between the bulk Sb_2Se_3 and Mo, which hinders the charge transport and leads to a high R_S. The device performances of SL-500 are superior in every parameter to that of any other device. The highest performance of the SL-500 device is attributed to the more desired crystal orientation in the [hkl, l≠0] directions (Figure 1f), because the grains in the [hkl, l≠0] favor charge transport throughout the film and lower recombination in the absorber layer. Particularly, an overall high EQE and an increase in the longer wavelength range (> 600 nm) indicate better absorber quality and improved back contact at the interface of

Mo and Sb_2Se_3 compared with the other two devices. Figure 3c-f compares the statistical distribution of the key PV parameters for these devices, showing the same trend as in the champion device comparison.

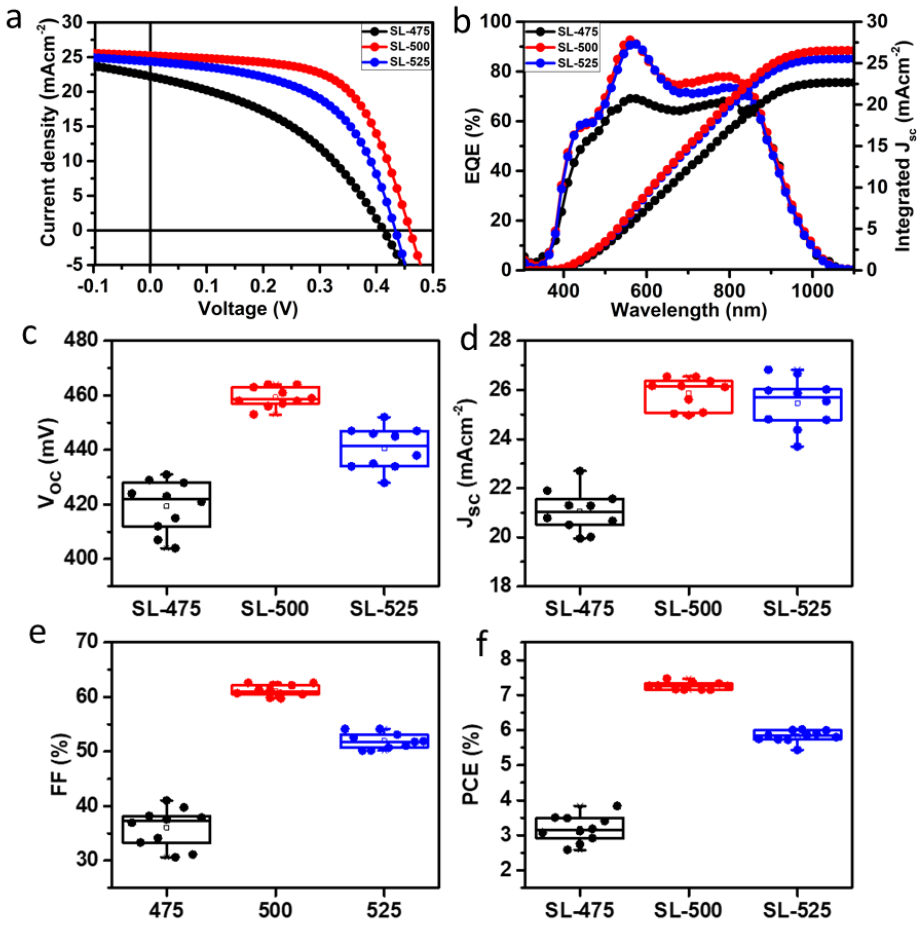

Figure 3. (a) J-V and (b) EQE curves of the champion Sb_2Se_3 solar cells grown on different seed layer conditions. (c-f) Statistical distributions of (c) V_{OC}, (d) J_{SC}, (e) FF and (f) PCE of Sb_2Se_3 solar cells grown on different seed layer conditions.

Table 1. PV parameters of champion Sb_2Se_3 solar cells for different seed layer conditions.

Samples	V_{OC} (mV)	J_{SC} ($mAcm^{-2}$)	FF (%)	PCE (%)	R_S (Ωcm^{-2})	R_{SH} (Ωcm^{-2})
SL-475	412	22.70	41.03	3.84	6.84	79.86
SL-500	459	26.54	61.39	7.47	3.81	310.74
SL-525	434	25.54	54.14	6.00	5.21	169.65

To better understand how the seed layer and grain orientation influence solar cell performance, we used a solar cell capacitance simulator (SCAPS)[35] to study the impact of bulk defect density, R_S, and R_{SH} on the PV performance of Sb_2Se_3 solar cells. The parameters used for the SCAPS modeling are adapted from the literature and listed in Table S3.[36-37] Because of the 1D crystal structure, detrimental defects are mainly distributed at the ends of the $(Sb_4Se_6)_4$ ribbons, while the sides are mostly self-passivated. The horizontal grains in the [hk0] directions typically introduce more defects at GBs in the bulk Sb_2Se_3 film, whereas the vertical grains in the [hkl, l≠0] directions mainly have defects at the top and rear surfaces. Therefore, the bulk defect density in a Sb_2Se_3 film is determined by the grain orientation. We simulated the J-V and EQE curves of Sb_2Se_3 solar cells with different bulk defect densities from 10^{15} to 10^{18} cm^{-3} (Figure S4) and found that bulk defect induced Shockley-Read-Hall (SRH) recombination is the most critical factor limiting the performance of solar cells. Additionally, the seed layer condition also affects R_S and R_{SH}, which can lower the PV performance of Sb_2Se_3 solar cells. Although simulation only reveals the trend of the changes in the parameters, the results are consistent with our conclusion that the seed layers play a vital role in obtaining the desired defect properties in the absorber layer and optimizing the Sb_2Se_3/Mo interface resistance, ultimately governing the performance of solar cells.

2.1. Defect passivation of Vertically Oriented Sb2Se3 Films

Defect passivation is particularly important for the vertically oriented Sb_2Se_3 films prepared by the seed layer templated growth. We carried out a series of post-deposition annealing experiments in ambient air to study the impact of annealing temperature on the film properties and device performance. The SEM morphological analysis shows that increasing the annealing temperature can significantly modify the surface morphology of Sb_2Se_3 (Figure S5). High contrast white patches appeared on the surface of the Sb_2Se_3 films after annealing at above 325 °C in ambient air. Increasing annealing temperature leads to a higher density of the white patches and eventually the formation of many prism-shaped grains at 375 °C. These structures are speculated to be associated with Sb_2O_3, which has a cubic crystal structure. Although the oxide phase was not resolved in the XRD measurement of the air-annealed films (Figure S6), likely due to the small number of oxides below the detection limit of the instrument, the formation of an oxide-rich surface is evidenced by the EDS results, where the O to Se ratio increases with increasing the annealing temperature (Table S4). The atomic percentage of O is much higher at the point of white patches than on the grain (Figure S7).

Post-deposition annealing in air significantly changes the electrical properties of the Sb_2Se_3 films. **Figure 4a-d** shows the conductive atomic force microscopic (C-AFM) analysis of the Sb_2Se_3 films without and with air annealing. The corresponding AFM morphological images are shown in Figure S8. The C-AFM results reveal that GBs of vertically orientated Sb_2Se_3 grains are generally more resistive than grain interiors. Such prominent characteristics are attributed to the lower charge carrier densities at the GBs, suggesting a self-passivation behavior on the sides of 1D $(Sb_4Se_6)_4$ ribbons. The film annealed at 350 °C in air (Figure 4b) exhibits more uniform and slightly lower electrical conductivity across the film than the as-prepared film (Figure 4a). The measurements were performed in the dark, and a reduced conductivity indicates a lower leakage current. It is also noted that some selenium particle remains on the top of the as-prepared film (Figure 4a, red circles), which hinder the local photocurrent generation and collection. The air annealing process removes the excess Se particle on the top of the film (Figure 4b), enabling a better heterojunction quality and a higher photocurrent. Additionally, the formation of oxides on the surface helps passivate the Sb_2Se_3 films.

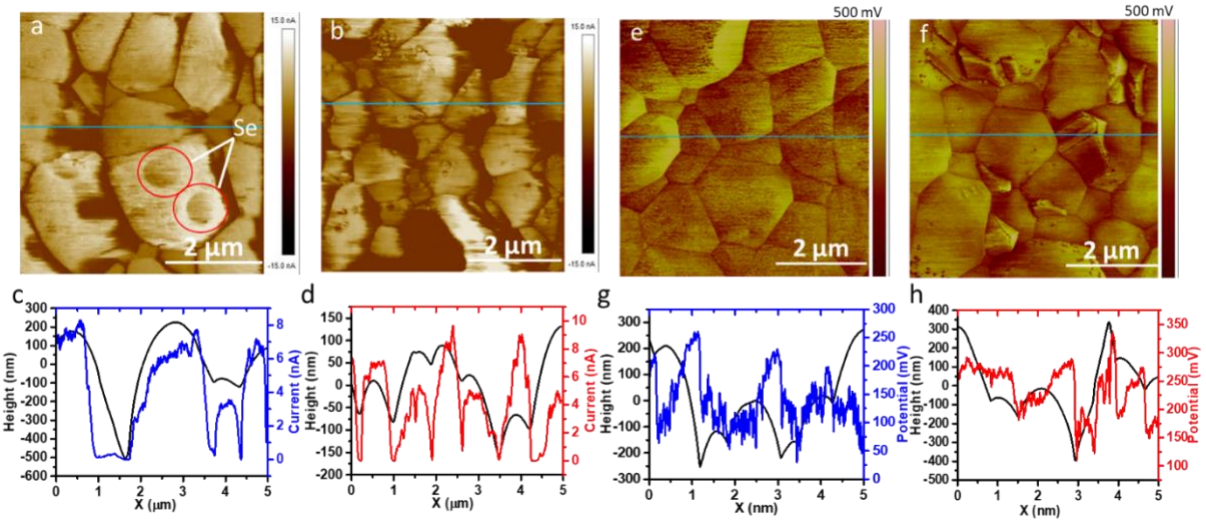

Figure 4. c-AFM and KPFM analysis of the Sb_2Se_3 films (a, e) without and (b, f) with air annealing at 350 ^oC. (c, d, g, h) The corresponding height profile and current/ surface potential of the films without and with annealing.

We further used the Kelvin probe force microscopy (KPFM) characterization to study the surface potential change in the films with and without air annealing. KPFM is a non-contact AFM method used to measure the surface potential. When we compare the surface potential between the two films, we found that the annealed film exhibits an overall ~100 mV higher surface potential than the as-prepared film (Figure 4e-h). The increased surface potential

corresponds to a lower work function (closer to the vacuum level), which can be contributed from both a larger downward band bending of the surface space charge region and a smaller electron affinity (χ_e) by the chemical and structural changes after annealing. If the increase in the surface band bending was solely responsible for the decrease in work function (W), the carrier concentration and electrical conduction would reduce to a factor of $\sim exp(-100\ mV/k_BT_r)=0.02$, assuming the mobility of charge carrier did not change significantly, where k_B is Boltzmann constant and T_r room temperature, respectively. The slight decrease in conductance could not account for the ~100 mV decreases in W and decrease in χ_e should attribute largely to the W change. This χ_e change could significantly reduce the conduction band offset (CBO) between Sb_2Se_3 and CdS (~360 mV in a spike shape),[38] benefiting the device performance. A schematic band diagram of the CdS/Sb_2Se_3 heterojunction interface is shown in Figure S9. In addition, the annealing could passivate the defects in both the near surface region (that would turn to interface region upon device completion) and in the film bulk. These annealing effects could be beneficial to reduce recombination and enhance junction quality of the Sb_2Se_3/CdS heterojunction, which plays an important role in improving the PCE of Sb_2Se_3 thin-film solar cells.

To validate the hypothesis that proper air-annealing is beneficial to solar cell performance, we fabricated a batch of devices using Sb_2Se_3 films prepared by the same optimal deposition procedures but post-annealed at different temperatures in air. The statistical comparison of PV parameters of the Sb_2Se_3 devices post-treated under different conditions is summarized in Figure S10. The result shows that 350 °C is the optimal annealing temperature. **Figure 5a** plots the J-V curves for the Sb_2Se_3 champion solar cells without and with air-annealing. The champion cell exhibits a PCE of 8.5%, with a high V_{OC} of 505 mV, a J_{SC} of 27.74 mA cm^{-2}, and a FF of 60.7, significantly outperforming the unannealed device. It is worth noting that the V_{OC} of 505 mV is among the highest reported value for Sb_2Se_3 solar cells (Table S1). A high V_{OC} is attributed to the desired Sb_2Se_3 crystal orientation, surface defect passivation, and better junction quality, consistent with the above-mentioned characterization results. Additionally, the EQE analysis (Figure 5b) shows better spectral responses at the longer wavelengths (700 to 1000 nm) after annealing in air, indicating the reduced SRH recombination and longer carrier lifetime. Despite the increased V_{OC} and $J_{SC,}$ we observed a slightly reduced FF, mainly due to the formation of oxides on the surface of the absorber layer. The formation of a resistive layer at the front interface leads to an increment in the R_S, although R_{SH} is slightly better due to the

passivation of the absorber layer (Table S5). Further optimization of this air-annealing process to balance the passivation and increased resistance will boost the PCE of the solar cells.

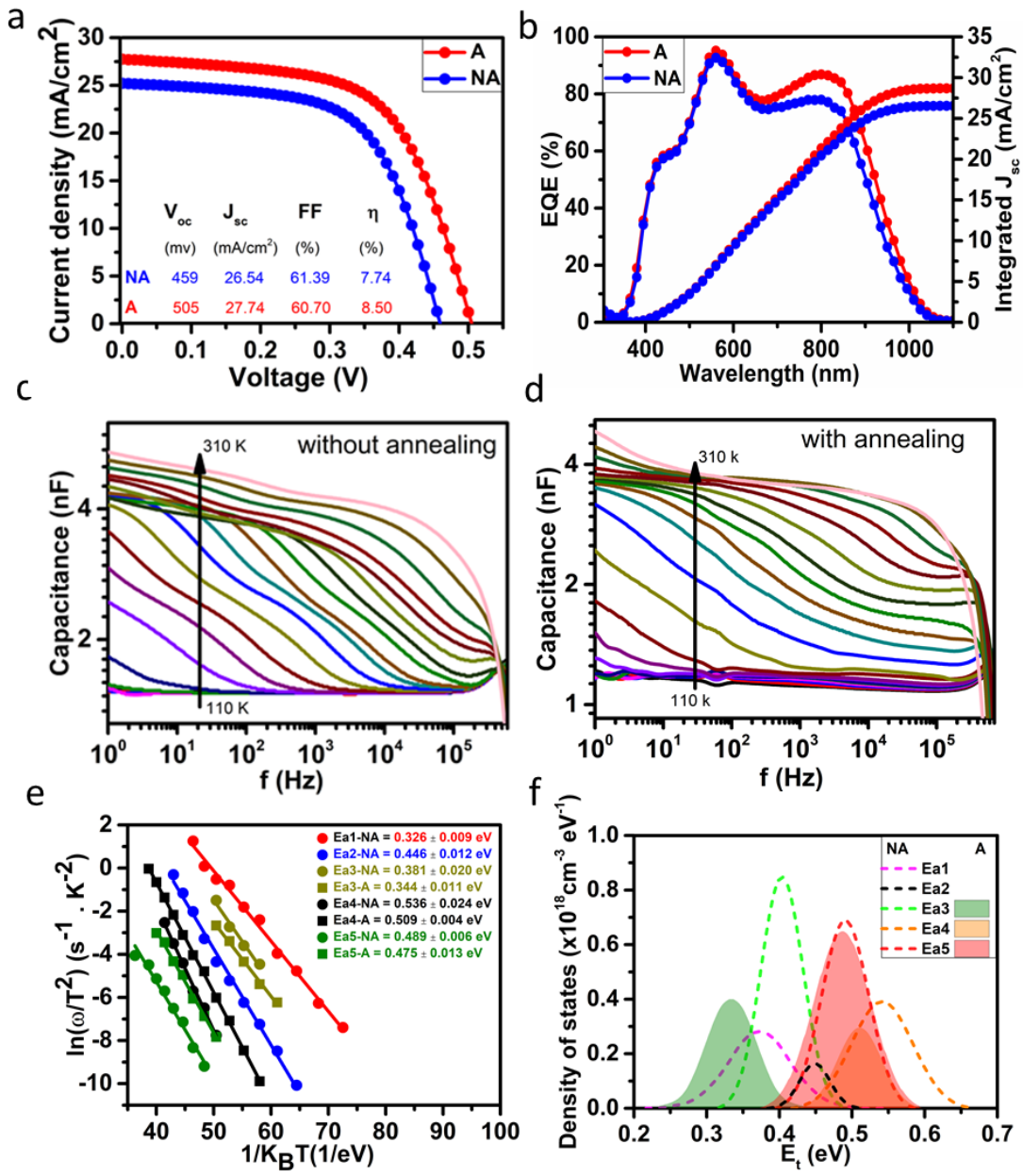

Figure 5. (a) J-V and (b) EQE curves of Sb_2Se_3 solar cells, with (A) and without (NA) air annealing. Temperature-dependent admittance spectra measured under dark equilibrium and temperature from 110 – 300 K with 10K temperature step size of Sb_2Se_3 solar cells, (c) with and (d) without air annealing, their corresponding (e) Arrhenius plots, and (f) defect distribution of the two devices.

To better understand the origins of device performance improvement, we conducted temperature-dependent admittance spectroscopy (TAS) measurement to study the defect

properties Sb_2Se_3 solar cells (Figure 5c-f). Temperature-dependent admittance (C-f-T) spectroscopy measurements were done in the temperature ranging from 110 to 310 K on our champion devices to reveal the distribution of defects and defect-induced carrier recombination mechanism. Figure 5c, d shows the C-f-T spectra for our devices without and with annealing. Figure S11 shows the differential capacitance spectra, in which the thermal activation energy is calculated by using the following equation[39]:

$$\omega_0 = A_0 T^2 exp\left[-\frac{E_a}{k_B T}\right] \quad (2)$$

where ω_0 is the characteristic transition frequency, T is the absolute temperature, k_B is the Boltzmann constant, A_0 is a pre-exponential constant, and E_a is the defect activation energy. The characteristic transition frequency of each capacitance signature is determined from the peak of the differential capacitance spectra (Figure S11c-e) and used to construct Arrhenius plots (Figure 5e). Based on equation 2, E_a is calculated from the linear fit of Arrhenius plots. Five characteristic activation energies (Ea1-NA, Ea2-NA, Ea3-NA, Ea4-NA, and Ea5-NA) are obtained for the samples without annealing, whereas three characteristics activations energies (Ea3-A, Ea4-A, and Ea5-A) are obtained for the samples with annealing (Figure 5e). Note that some defect states exhibit similar defect energy levels but distinctive characteristic frequency responses. The activation energies, frequencies, temperatures of these defects are listed in Table S6.

Figure 5f shows the defect distribution of each defect type, in which the defect energy distribution ($E_t(\omega)$) with respect to the valence band and the defect density of states ($N_t\big(E(\omega)\big)$) as a function of angular frequency ω are obtained by the following equations [39] :

$$E_t(\omega) = E_a - k_B T ln\left(\frac{\omega_0}{\omega}\right) \quad (3)$$

$$N_t\big(E(\omega)\big) = \frac{V_{bi}}{qWk_BT}\left(-\omega\frac{dC}{d\omega}\right) \quad (4)$$

where V_{bi} and W are the built-in potential and depletion width of the p-n junction, respectively, extracted from the Mott-Schottky analysis of the capacitance-voltage measurements. The energetic distribution of the defect density of states is obtained by the Gaussian fit. Table S7 lists the calculated density of states for each defect.

Sb_2Se_3 thin films can have different point defects on the basis of two growing conditions, including Se-rich and Se-poor conditions. Under the Se-poor condition, two detrimental donor defects Sb_{Se} and V_{Se} are easily formed, whereas Se_{Sb}, Se_i, and V_{Sb} defects are preferably formed under the Se-rich condition.[9] According to the EDS analysis (Table S3), our devices are slightly Se-poor. Therefore, we expect that Sb_{Se} and V_{Se} are major defects in our Sb_2Se_3 films.

However, the complexity of the defect physics of Sb_2Se_3 and the discrepancy between the experimental and theoretical results make it difficult to assert the identity of the defects.[9, 40-42] Nonetheless, our TAS analysis reveals a number of defect states coexisting in the Sb_2Se_3 absorber layer. Further studies are needed to clarify the origins and identities of these defects.

Comparing the activation energy and defect distribution for unannealed and annealed Sb_2Se_3 devices, we found that the total number of defect levels was reduced from five to three, the total defect density of all levels was decreased by ~ 38%, and defect activation energies were lower after air annealing, indicating that some of the defects are completely and partially passivated, and others become shallower. The reduced defect densities and lower defect energy levels are mainly attributed to the oxygen passivation on the defects because oxygen can fill V_{Se} and form bonding with both under coordinated Sb and Se atoms. We also compared the defect capture cross-section of the two samples (Table S8). The annealing device exhibits lower capture cross-section valves compared with the unannealed one, indicating reduced recombination in the absorber layer. Such defect passivation is beneficial to the PV performance of the devices.

TAS measurements at various DC biases with a constant AC modulation were performed to determine if these defects belong to bulk or interface defects. When the activation energy varies with DC bias, the defect is an interface defect. On the contrary, if the activation energy remains constant with changing the DC bias, the defect is a bulk defect. Figure S12 shows that all the activation energies in both annealed and unannealed samples are bias-independent, suggesting that these defects are located in the bulk of the Sb_2Se_3 absorbers. Overall, the TAS measurement results confirm the bulk defects in the Sb_2Se_3 absorber are passivated after the annealing in air.

We also measured the dark J-V curves of the Sb_2Se_3 cells without and with annealing at various temperatures. The annealed cell shows a dark saturation current density (J_0) of 3.14×10^{-7} mA cm^{-2} (Figure S13a-b) which is lower than J_0 of 9.9×10^{-7} mA cm^{-2} for the unannealed cells. The reduced J_0 confirms the reduced SRH recombination measured by TAS, enabling a high V_{OC} exceeding 500 mV for the air-annealed device. The Arrhenius plots of $\ln(J_0/T^2)$ as a function of the reciprocal of the thermal energy (Figure S13c) show the same activation energy ($q\phi$) for both annealed and unannealed devices, indicating no change in the interface barrier in these two devices. This result confirms that the oxygen-assisted defect passivation is mainly impacting the bulk defects while it does not alter the interfacial properties.

3. Conclusion

In summary, we investigated the seed layer preparation condition to achieve the templated growth of vertically oriented Sb_2Se_3 films on Mo coated glass substrates. After the optimization

of the grain orientation, crystallinity, and rear interface properties, we obtained a champion PCE of 7.47% for substrate-type Sb_2Se_3 solar cells. We then employed post-deposition annealing in air to passivate bulk defects in the Sb_2Se_3 absorber layer. The air annealing effectively reduces the densities of the defects and lowers their activation energies, resulting in lower J_0 and higher PCE. As a result, our best-performing device after annealing in air delivers a PCE of 8.5%. This work demonstrates a facile and effective approach to preparing high-performance Sb_2Se_3 solar cells.

4. Experimental Methods

Substrate preparation: Sb_2Se_3 seed and bulk layers were prepared on Mo coated soda lime glass substrate by rapid thermal evaporation (RTE) and closed space sublimation (CSS) methods, respectively. First, glass substrates were cleaned by using detergent solution (Micro-90) and deionized (DI) water in an ultrasonic bath and dried by nitrogen blowing. Then, a bilayer Mo film was deposited by direct current (DC) sputtering in an argon (Ar) environment in a two-step process, consisting of a high working pressure of 15 mT for the adhesion layer and a low working pressure of 4 mT for the bulk Mo film. The total thickness of Mo is ~ 900 nm.

Deposition of Sb_2Se_3 thin films: we prepared a source plate by using high purity Sb_2Se_3 powders (Jiangxi Ketai Advanced Materials Co. Ltd.). A several microns thick Sb_2Se_3 film was deposited on a graphite plate at a base pressure of 5 mT by keeping the substrate temperature (T_{sub}) at 350 °C and source temperature (T_{sou}) at 560 °C for half an hour in a CSS system.[14, 20] The main purpose of making a source plate is to control the sublimation rate. A spacer with a height of 6 mm was used between the source plate and the Mo coated glass substrates. Sb_2Se_3 absorber layers were deposited by a two-step process. The substrate and Sb_2Se_3 source plate were first preheated at 315 °C for 5 min using Infrared (IR) heaters. Sb_2Se_3 seed layers were deposited at different source temperatures ranging from 475 to 525 °C using an RTE approach (Figure S1), i.e., ramping up the source temperature to the setpoint and immediately cooling down to room temperature naturally while maintaining pressure at 230 mTorr. We placed a graphite plate on the top of Mo substrates to maintain uniform temperature on the Mo substrates during the sublimation process. After absorbing the infrared light from the IR heaters, Sb_2Se_3 powders evaporated and formed a thin seed layer on the Mo substrates. During the deposition, T_{sub} was kept constant at 315 °C. Note that increasing T_{sou} also increases T_{sub} unintentionally. T_{sub} increased to 340, 370, and 400 °C when T_{sou} were set to 475, 500, and 525 °C, respectively. After that, a bulk Sb_2Se_3 layer was

deposited on top of the seed layer by CSS method where T_{sou} was at 480 °C, and T_{sub} was at 400 °C. The deposition was carried out under a nitrogen flow at 400 sccm and a base pressure of 230 mT. The total deposition time was 6 min, and the thickness of Sb_2Se_3 absorber layers was ~2 μm. The obtained absorber layers were selenized at 425 °C in Ar with 50 mg selenium powders to improve the crystallization of the Sb_2Se_3 films. Note, all the devices studied in this paper are selenized.

Device fabrication: After the selenization, Sb_2Se_3 thin films were annealed on a hot plate in ambient air at different temperatures for 1 min. After the annealing of Sb_2Se_3 thin films, a 55 nm CdS buffer layer was deposited on the top of crystallized Sb_2Se_3 films using chemical bath deposition (CBD), following the method reported elsewhere.[14] A 50 nm intrinsic ZnO (iZO) layer and a 250 nm aluminum-doped zinc oxide (AZO) front contact layer were deposited sequentially by radiofrequency (rf) sputtering at a power of 100 and 150 W, respectively, in a Lesker deposition system. Lastly, a 200 nm Ag was deposited on the AZO layer via thermal evaporation to form a metal grid. The completed film stacks were separated into individual cells (0.2 cm^2) by mechanically scribing. Devices were categorized into four groups: SL-475, SL-500, SL-525, and SL-NS according to the seed layer deposition conditions. Here, SL-475 denotes a device whose seed layer was deposited at T_{sou} of 475 ˚C. Similarly, SL-500, and SL-525, represent devices with the seed layers deposited at 500 and 525 ˚C, respectively. SL-NS denotes the devices prepared without a seed layer. The structural schematic diagram of Sb_2Se_3 solar cells and the RTE equipment are shown in Figure S1.

Measurement and characterization: X-ray diffraction (XRD, Rigaku Ultima III, Cu Kα radiation under operation conditions of 40 kV and 44 mA) was used to analyze the crystal structure of Sb_2Se_3 films. The morphology of the Sb_2Se_3 films was characterized by using high-resolution field emission scanning electrons microscopy (FE-SEM, Hitachi S-4800) equipped with X-ray energy dispersive spectroscopy (EDS). Performance of the solar cells was measured using density-voltage (J-V) curves under AM1.5 illumination by a LED solar simulator (Newport) and a source meter (Keithley 2400) at a scanning speed of 1.17 V/s. QE system (PV Measurement Beaverton, OR, USA) was used to measure the external quantum efficiency (EQE) spectra. Kelvin probe force microscopy (KPFM) was performed on a home-built KPFM system based on D3100 atomic force microscope (AFM). Conductive AFM was performed on a Bruker Dimension Icon system. Pt-Ir-coated silicon probes (Nano sensor PPP-EFM) were used in both measurements. The scan size is 5 × 5 μm^2 that contains 1024 × 256 pixels. TAS and J-V-T measurements were done by Modulab potentiostat equipped with a frequency response analyzer (Ametek Inc.). All the setup, experiments, and results were obtained by using

a Modulabl system and XM-studio software. TAS was performed under a constant AC modulation voltage of 45 mV_{rms}. Frequency sweeping from 1.0 MHz to 0.1 Hz was used for the TAS measurement. During TAS measurement, DC biases varying from -0.3 to 0.2 V at a step size of 0.1 V. J-V-T measurements were scanned with DC biases varying from 0.0 to 0.9 V. All the temperature-dependent measurements were done by using a liquid-nitrogen cooled cryogenic system (Janis VPF-100). A temperature controller (Lakeshore 330) was used to control the temperature. To make sure that the recorded temperature is from the samples, a temperature sensor was mounted directly on the top of the device.

Supporting Information

Supporting Information is available from the Wiley Online Library or from the author.

Acknowledgements

This material is based on research sponsored by the U.S. Air Force Research Laboratory under agreement numbers FA9453–18-2–0037 and FA9453–19-C-1002. The U.S. Government is authorized to reproduce and distribute reprints for Governmental purposes not withstanding any copyright notation thereon. Disclaimer: The views and conclusions contained herein are those of the authors and should not be interpreted as necessarily representing the official policies or endorsements, either expressed or implied, of the U.S. Air Force Research Laboratory or the U.S. Government.

Conflict of Interest

The authors declare no conflict of interest.

Received: ((will be filled in by the editorial staff))
Revised: ((will be filled in by the editorial staff))
Published online: ((will be filled in by the editorial staff))

References

[1] K. Zeng, D.-J. Xue, J. Tang, Semiconductor Science and Technology 2016, 31, 063001.

[2] N. K. Jayswal, S. Rijal, B. Subedi, I. Subedi, Z. Song, R. W. Collins, Y. Yan, N. J. Podraza, Solar Energy 2021, 228, 38.

[3] T. Tanaka, T. Sueishi, K. Saito, Q. Guo, M. Nishio, K. M. Yu, W. Walukiewicz, Journal of Applied Physics 2012, 111, 053522.

[4] H. Xie, M. Dimitrievska, X. Fontané, Y. Sánchez, S. López-Marino, V. Izquierdo-Roca, V. Bermúdez, A. Pérez-Rodríguez, E. Saucedo, Solar Energy Materials and Solar Cells 2015, 140, 289.

[5] N. Fleck, O. S. Hutter, L. J. Phillips, H. Shiel, T. D. C. Hobson, V. R. Dhanak, T. D. Veal, F. Jäckel, K. Durose, J. D. Major, ACS Appl. Mater. Interfaces 2020, 12, 52595.

[6] X. Liu, J. Chen, M. Luo, M. Leng, Z. Xia, Y. Zhou, S. Qin, D.-J. Xue, L. Lv, H. Huang, ACS Appl. Mater. Interfaces 2014, 6, 10687.

[7] Z. Li, X. Liang, G. Li, H. Liu, H. Zhang, J. Guo, J. Chen, K. Shen, X. San, W. Yu, R. E. I. Schropp, Y. Mai, Nature Communications 2019, 10, 125.

[8] W. Shockley, H. J. Queisser, J. Appl. Phys. 1961, 32, 510.

[9] X. Liu, X. Xiao, Y. Yang, D. J. Xue, D. B. Li, C. Chen, S. Lu, L. Gao, Y. He, M. C. Beard, G. Wang, S. Chen, J. Tang, Progress in Photovoltaics: Research and Applications 2017, 25, 861.

[10] K. Li, C. Chen, S. Lu, C. Wang, S. Wang, Y. Lu, J. Tang, Advanced Materials 2019, 31, 1903914.

[11] K. Shen, Y. Zhang, X. Wang, C. Ou, F. Guo, H. Zhu, C. Liu, Y. Gao, R. E. I. Schropp, Z. Li, X. Liu, Y. Mai, Advanced Science 2020, 7, 2001013.

[12] X. Liu, C. Chen, L. Wang, J. Zhong, M. Luo, J. Chen, D.-J. Xue, D. Li, Y. Zhou, J. Tang, Progress in Photovoltaics: Research and Applications 2015, 23, 1828.

[13] X. Wen, C. Chen, S. Lu, K. Li, R. Kondrotas, Y. Zhao, W. Chen, L. Gao, C. Wang, J. Zhang, Nature communications 2018, 9, 2179.

[14] D.-B. Li, X. Yin, C. R. Grice, L. Guan, Z. Song, C. Wang, C. Chen, K. Li, A. J. Cimaroli, R. A. Awni, D. Zhao, H. Song, W. Tang, Y. Yan, J. Tang, Nano Energy 2018, 49, 346.

[15] G. Liang, X. Chen, D. Ren, X. Jiang, R. Tang, Z. Zheng, Z. Su, P. Fan, X. Zhang, Y. Zhang, S. Chen, Journal of Materiomics 2021.

[16] Y. Ma, B. Tang, W. Lian, C. Wu, X. Wang, H. Ju, C. Zhu, F. Fan, T. Chen, Journal of Materials Chemistry A 2020, 8, 6510.

[17] Z. Li, X. Chen, H. Zhu, J. Chen, Y. Guo, C. Zhang, W. Zhang, X. Niu, Y. Mai, Solar Energy Materials and Solar Cells 2017, 161, 190.

[18] M. Leng, M. Luo, C. Chen, S. Qin, J. Chen, J. Zhong, J. Tang, Applied Physics Letters 2014, 105, 083905.

[19] G.-X. Liang, Y.-D. Luo, S. Chen, R. Tang, Z.-H. Zheng, X.-J. Li, X.-S. Liu, Y.-K. Liu, Y.-F. Li, X.-Y. Chen, Z.-H. Su, X.-H. Zhang, H.-L. Ma, P. Fan, Nano Energy 2020, 73, 104806.

[20] S. Rijal, D.-B. Li, R. A. Awni, S. S. Bista, Z. Song, Y. Yan, ACS Applied Energy Materials 2021, 4, 4313.

[21] S. Rijal, Z. Song, D. B. Li, S. S. Bista, Y. Yan, "Optimizing the Selenization of Sb2Se3 Absorbers to Improve the Film Quality and Solar Cell Performances", presented at 2021 IEEE 48th Photovoltaic Specialists Conference (PVSC), 20-25 June 2021, 2021.

[22] C. Chen, K. Li, S. Chen, L. Wang, S. Lu, Y. Liu, D. Li, H. Song, J. Tang, ACS Energy Letters 2018, 3, 2335.

[23] C. Ou, K. Shen, Z. Li, H. Zhu, T. Huang, Y. Mai, Solar Energy Materials and Solar Cells 2019, 194, 47.

[24] G. Li, Z. Li, X. Liang, C. Guo, K. Shen, Y. Mai, ACS Appl. Mater. Interfaces 2019, 11, 828.

[25] O. S. Hutter, L. J. Phillips, K. Durose, J. D. Major, Solar Energy Materials and Solar Cells 2018, 188, 177.

[26] R. Kondrotas, J. Zhang, C. Wang, J. Tang, Solar Energy Materials and Solar Cells 2019, 199, 16.

[27] L. Guo, B. Zhang, Y. Qin, D. Li, L. Li, X. Qian, F. Yan, Solar RRL 2018, 2, 1800128.

[28] C.-J. Tong, K. P. McKenna, The Journal of Physical Chemistry C 2019, 123, 23882.

[29] B. A. Korevaar, J. R. Cournoyer, O. Sulima, A. Yakimov, J. N. Johnson, Progress in Photovoltaics: Research and Applications 2014, 22, 1040.

[30] F. Werner, B. Veith-Wolf, C. Spindler, M. R. Barget, F. Babbe, J. Guillot, J. Schmidt, S. Siebentritt, Physical Review Applied 2020, 13, 054004.

[31] X. Cui, K. Sun, J. Huang, J. S. Yun, C.-Y. Lee, C. Yan, H. Sun, Y. Zhang, C. Xue, K. Eder, L. Yang, J. M. Cairney, J. Seidel, N. J. Ekins-Daukes, M. Green, B. Hoex, X. Hao, Energy & Environmental Science 2019, 12, 2751.

[32] L. Guo, B. Zhang, S. Li, A. Montgomery, L. Li, G. Xing, Q. Zhang, X. Qian, F. Yan, Materials Today Physics 2019, 10, 100125.

[33] C. Chen, D. C. Bobela, Y. Yang, S. Lu, K. Zeng, C. Ge, B. Yang, L. Gao, Y. Zhao, M. C. Beard, J. Tang, Frontiers of Optoelectronics 2017, 10, 18.

[34] X. Liang, X. Chen, Z. Li, G. Li, J. Chen, L. Yang, K. Shen, Y. Xu, Y. Mai, Applied Physics A 2019, 125, 381.

[35] M. Burgelman, P. Nollet, S. Degrave, Thin Solid Films 2000, 361–362, 527.

[36] A. Basak, U. P. Singh, Solar Energy Materials and Solar Cells 2021, 230, 111184.

[37] Z.-Q. Li, M. Ni, X.-D. Feng, Materials Research Express 2020, 7, 016416.

[38] H. Shiel, O. S. Hutter, L. J. Phillips, J. E. N. Swallow, L. A. H. Jones, T. J. Featherstone, M. J. Smiles, P. K. Thakur, T.-L. Lee, V. R. Dhanak, J. D. Major, T. D. Veal, ACS Applied Energy Materials 2020, 3, 11617.

[39] J. V. Li, G. Ferrari, "Capacitance spectroscopy of semiconductors", 2018.

[40] T. D. C. Hobson, L. J. Phillips, O. S. Hutter, K. Durose, J. D. Major, Applied Physics Letters 2020, 116, 261101.

[41] Christopher N. Savory, D. O. Scanlon, Journal of Materials Chemistry A 2019, 7, 10739.

[42] M. Huang, P. Xu, D. Han, J. Tang, S. Chen, ACS Appl. Mater. Interfaces 2019, 11, 15564.